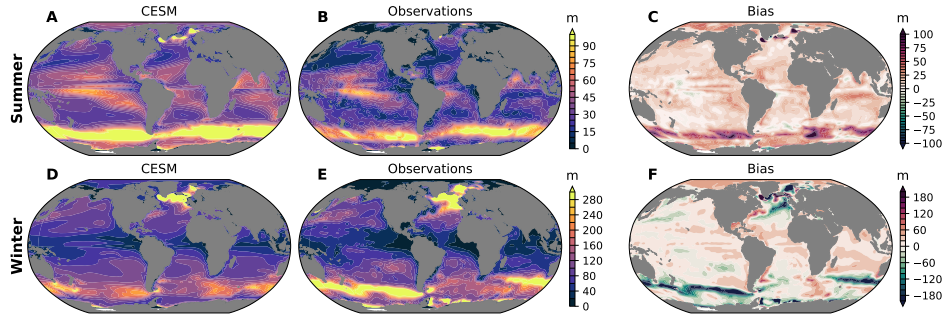

Figure 1. Climatological mixed layer depth (A,D) simulated by CESM2 over 1990–2014 compared with (B,F) observationally-based estimates of mixed layer depth from WOA2013. The right column shows model biases (C,F). Mixed layer depth was computed using a $\Delta_{\sigma_\theta} = 0.125$ criterion (Monterey & Levitus, 1997). The top row shows summertime distributions, which correspond to June–August means in the Northern Hemisphere and December–February means in the Southern Hemisphere (A-C). These seasons are reversed for each hemisphere in the bottom row, which shows winter (D-F).

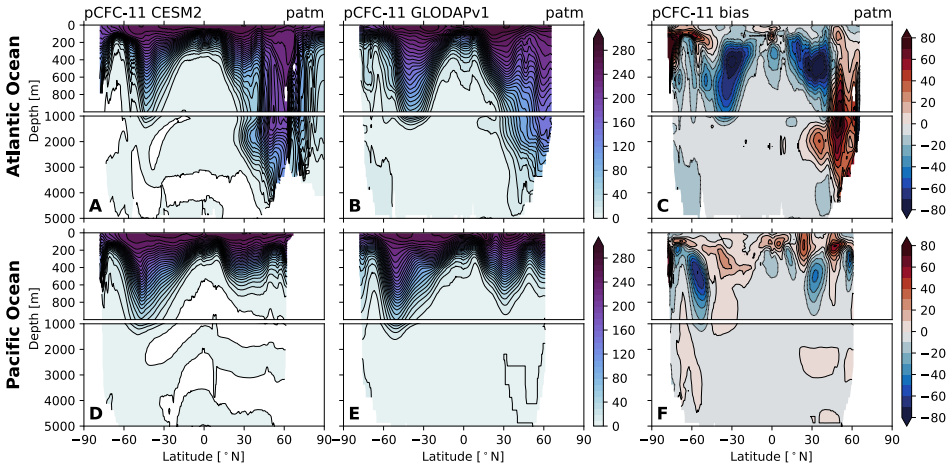

Figure 2. CESM-simulated zonal-mean partial pressure of CFC-11 (pCFC-11) for 1990–2000 (A,D) compared with observations from GLODAPv1 (B,E) (Key et al., 2004). The right column shows model biases (C,F). The top row is the distributions for the Atlantic Ocean (A-C) and the bottom row is the Pacific Ocean distributions (D-F).

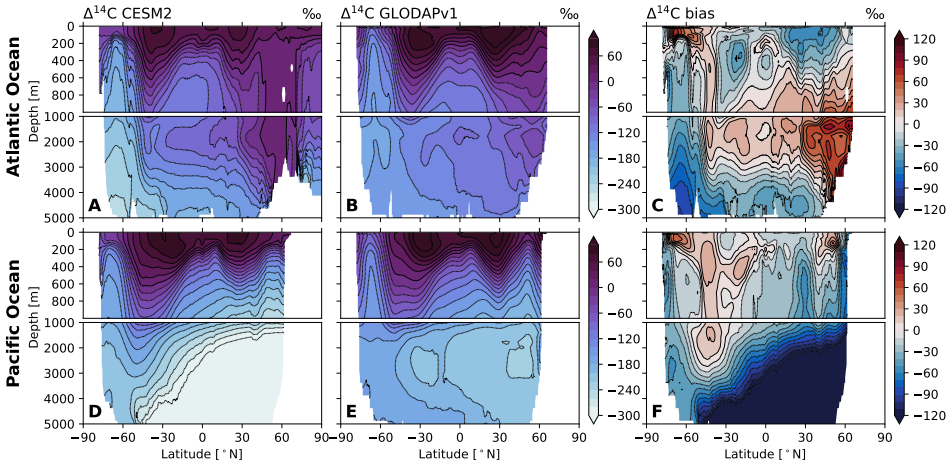

Figure 3. CESM-simulated zonal-mean radiocarbon (^{14}C) distributions for 1990–2000 (A,D) compared with observations from GLODAPv1 (B,E) (Key et al., 2004). The right column shows model biases (C,F). The top row is the distributions for the Atlantic Ocean (A-C) and the bottom row is the Pacific Ocean distributions (D-F).

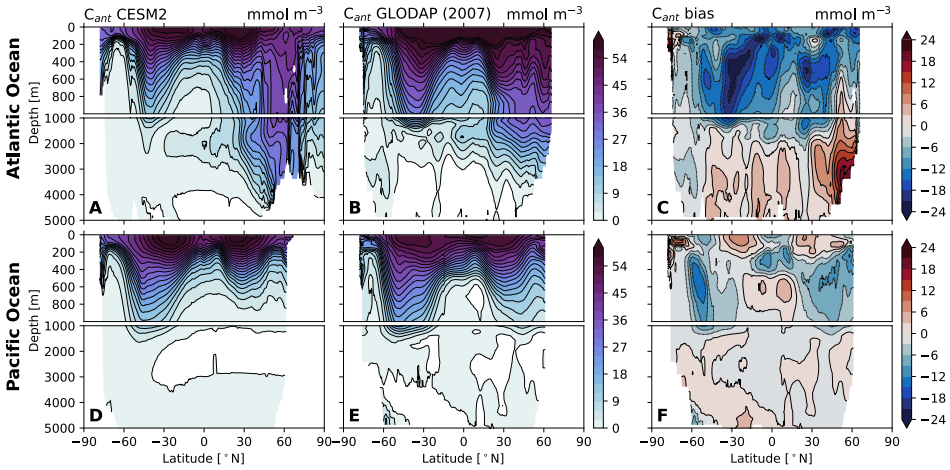

Figure 4. CESM-simulated zonal-mean anthropogenic carbon inventory (C_{ant}) for 2007 (A,D) compared with observations from GLODAPv1 (B, E) (Key et al., 2004) and adjusted for uptake between 1994–2007 (Gruber et al., 2019). The right column shows model biases (C,F). The top row is the distributions for the Atlantic Ocean (A-C) and the bottom row is the Pacific Ocean distributions (D-F).

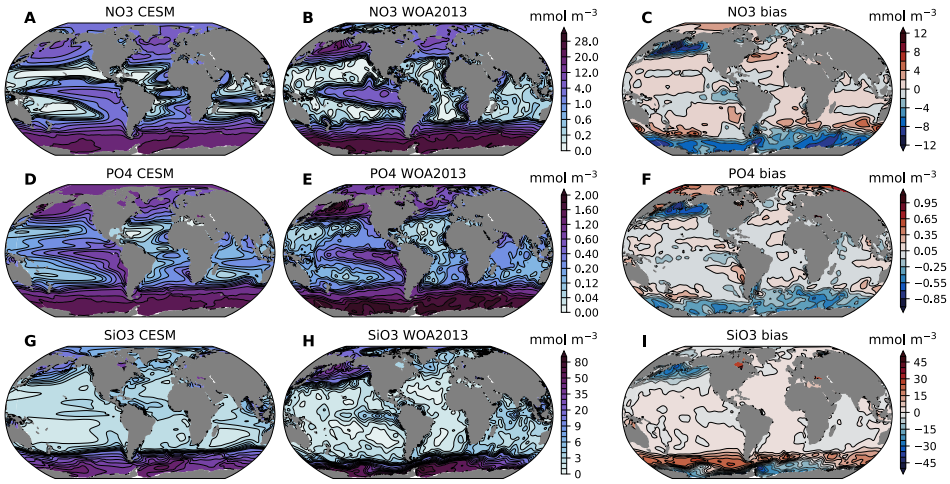

Figure 5. CESM simulated annual mean surface nitrate (A), phosphate (D), and silicate concentrations (G) for 1990–2014 compared with observations from the World Ocean Atlas, 2018 (B,E,H) (Garcia et al., 2018). Note non-linear color scales. The right column shows model biases (C,F,I).

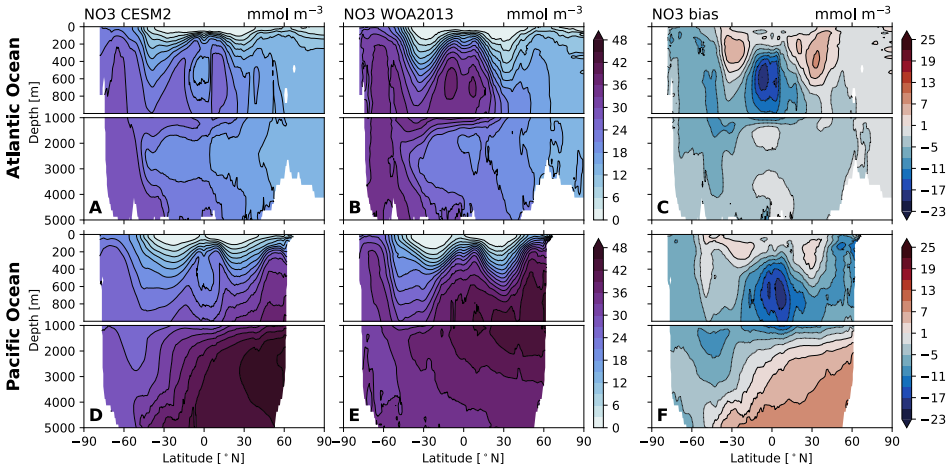

Figure 6. CESM-simulated annual mean of zonal-mean nitrate (NO_3) distributions for 1990–2014 compared with the World Ocean Atlas, 2018 (Garcia et al., 2018) (B,E). The right column shows model biases (C,F). The top row is the distributions for the Atlantic Ocean (A-C) and the bottom row is the Pacific Ocean distributions (D-F).

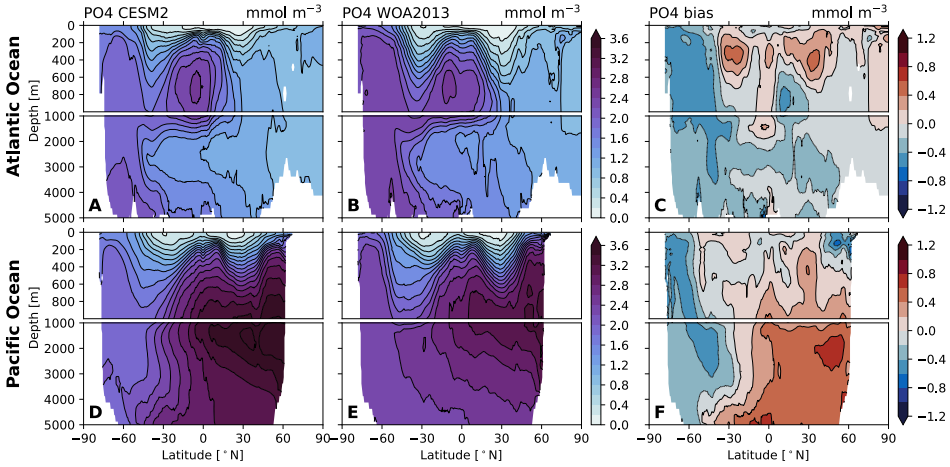

Figure 7. CESM simulated annual mean, zonal-mean phosphate for 1990–2014 compared with World Ocean Atlas, 2018 (Garcia et al., 2018) (B,E). The right column shows model biases (C,F). The top row is the distributions for the Atlantic Ocean (A-C) and the bottom row is the Pacific Ocean distributions (D-F).

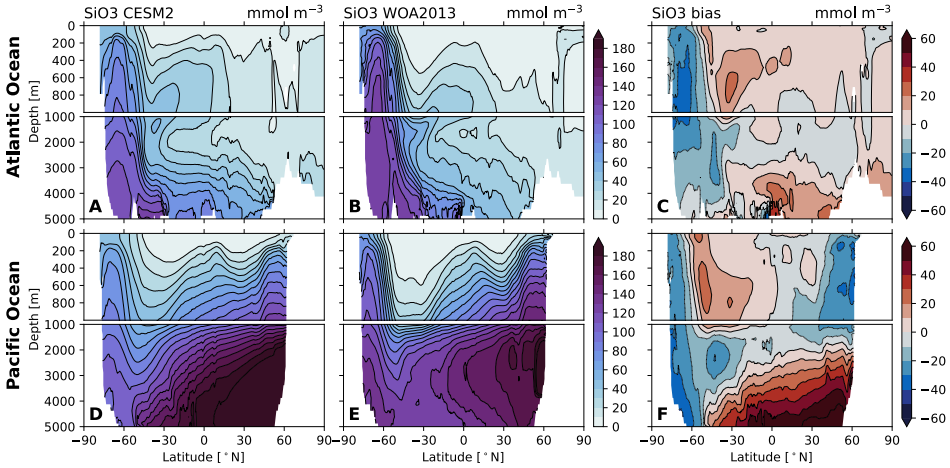

Figure 8. CESM simulated annual mean, zonal-mean silicate for 1990–2014 compared with observations from the World Ocean Atlas, 2018 (Garcia et al., 2018) (B,E). The right column shows model biases (C,F). The top row is the distributions for the Atlantic Ocean (A-C) and the bottom row is the Pacific Ocean distributions (D-F).

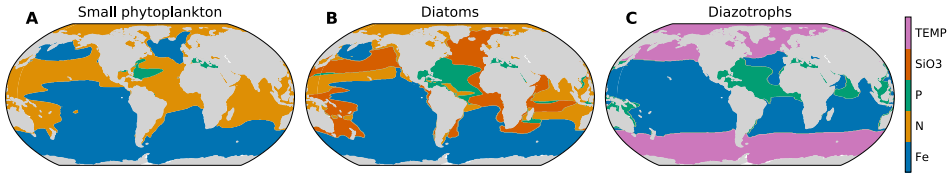

Figure 9. The factor most limiting phytoplankton growth for annual means over the period 1990–2014. Limitation terms (with the exception of temperature) are computed as biomass-weighted vertical averages. The temperature term for diazotrophs is approximated by applying the temperature threshold for growth (15°C) to annual-mean sea surface temperature.

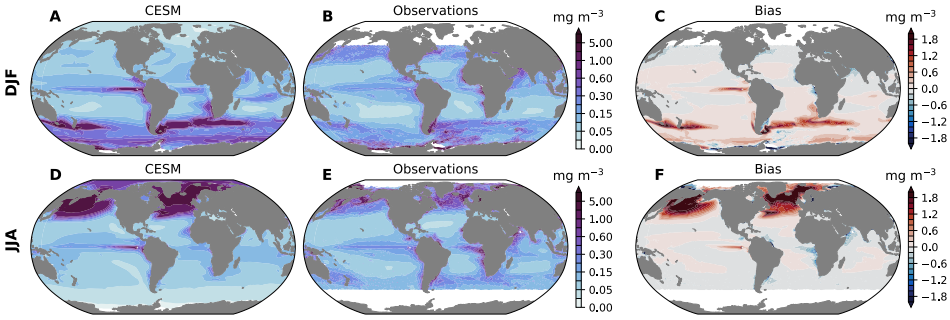

Figure 10. A comparison of SeaWiFS satellite derived chlorophyll concentration to CESM-simulated surface chlorophyll (top 10 m). The top row shows December-January-February (DJF) means, while the bottom row shows June-July-August (JJA) means. SeaWiFS observations are a mean over the period 1997 to 2010, while model means computed over the period 1990 to 2014.

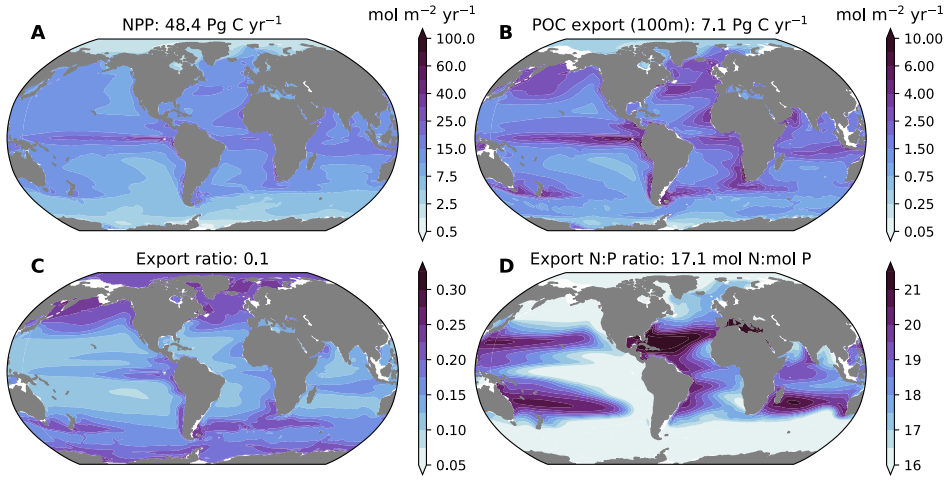

Figure 11. Net primary production (NPP) and organic matter export in CESM2 over the period 1990–2014. (A) NPP and (B) particulate organic matter (POC) export at 100 m in mol m^{-2} yr^{-1}, with globally integrated values indicated in the title of each panel. (C) The export ratio (i.e., pe-ratio = sinking export/NPP) and (D) the N:P ratio of exported biomass, with global mean values indicated in title of each panel.

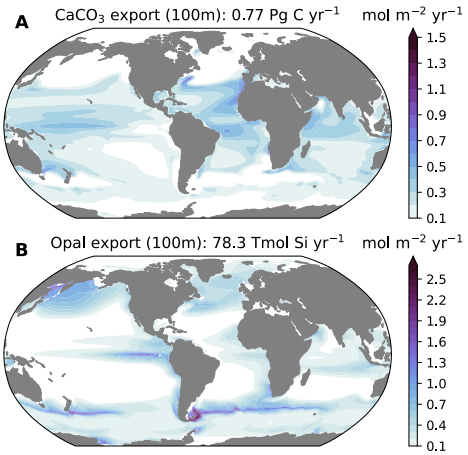

Figure 12. Mineral fluxes in CESM2 over the period 1990–2014. (A) $CaCO_3$ export at 100 m; (B) opal export at 100 m. Globally-integrated fluxes are indicated in the title above each panel.

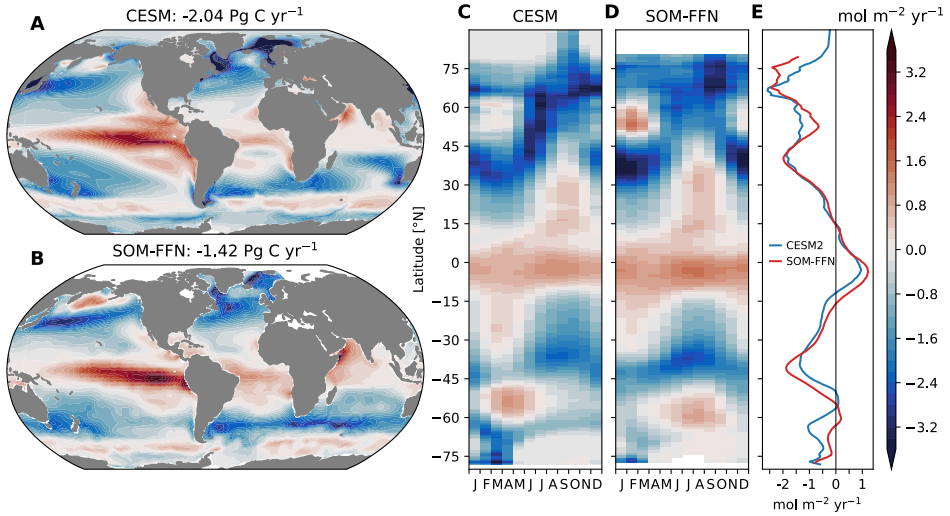

Figure 13. Air-sea CO_2 flux. (A) Simulated annual-mean air-sea CO_2 flux from CESM2 over the period 1990–2014. (B) Observationally-based estimate of air-sea CO_2 (Landschützer et al., 2017) based on the method of Landschützer et al. (2016).

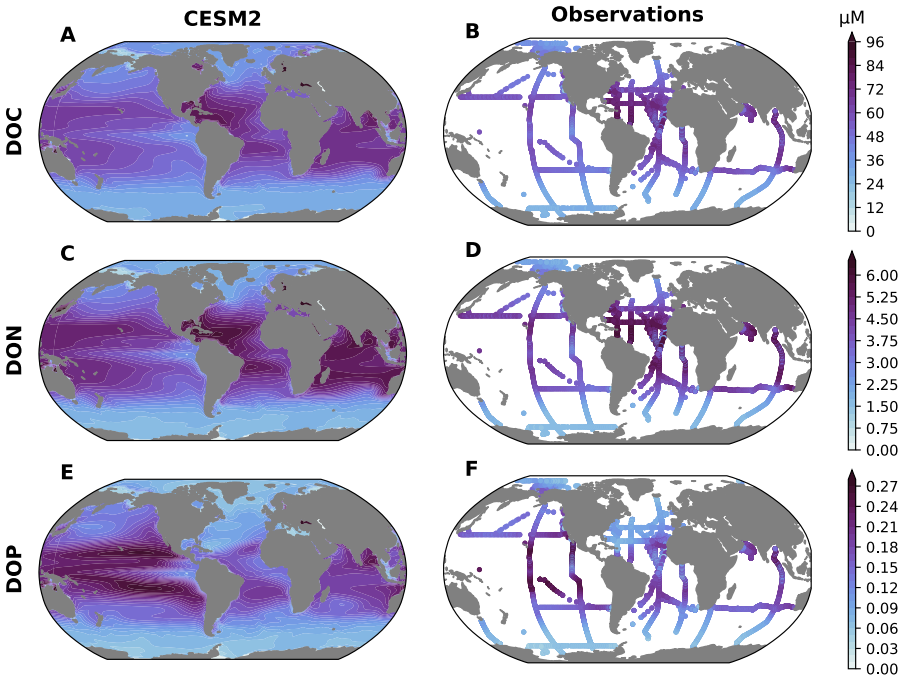

Figure 14. Simulated (left) and observed (right) concentrations of dissolved organic matter (µM) in the upper 100 m. (A, B) dissolved organic carbon; (C, D) dissolved organic nitrogen; (E, F) dissolved organic phosphorus. The observations are from Letscher and Moore (2015).

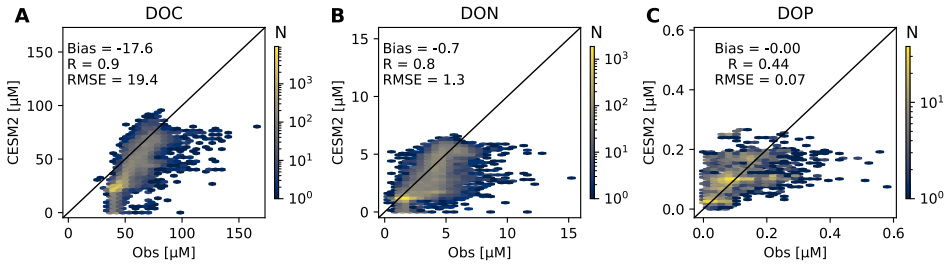

Figure 15. Comparison of simulated dissolved organic matter concentrations with observations over the upper 1000 m of the water column. Two-dimensional histograms of simulated versus observed concentrations (µM) for (A) dissolved organic carbon; (B) dissolved organic nitrogen; (C) dissolved organic phosphorus. Colors show the number of model-observation pairs in each bin; the black diagonal line shows a 1:1 relationship; inset text indicates mean bias, correlation, and root mean squared error (RMSE). The observations are from Letscher and Moore (2015).

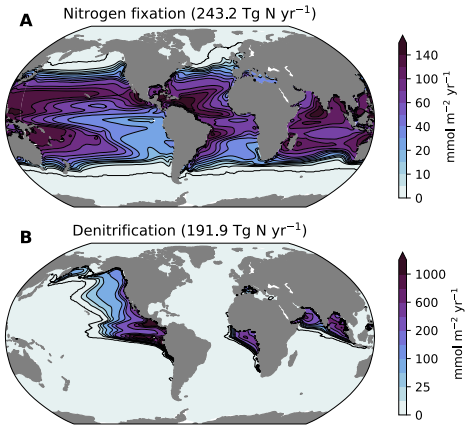

Figure 16. Annual mean (A) nitrogen fixation and (B) water column denitrification simulated by CESM2 for the period 1990–2014. Global integrals are reported in the figure titles.

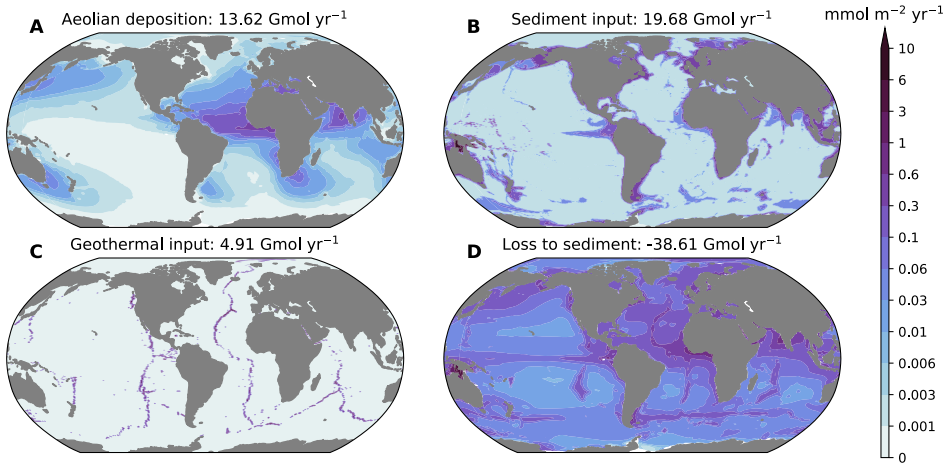

Figure 17. Spatial distribution of dominant terms in the CESM2 global iron budget. (A) Atmospheric deposition; (B) total sedimentary input, include oxic and reducing sedimentary sources; (C) geothermal input; (D) losses to sediments via burial. The title string of each panel reports the global integral. Note that the atmospheric deposition term includes a subsurface contribution from iron released when sinking dust is remineralized. This contribution accounts for 5.5 Gmol yr^{-1}. Riverine inputs are not shown; these account for 0.37 Gmol yr^{-1}.

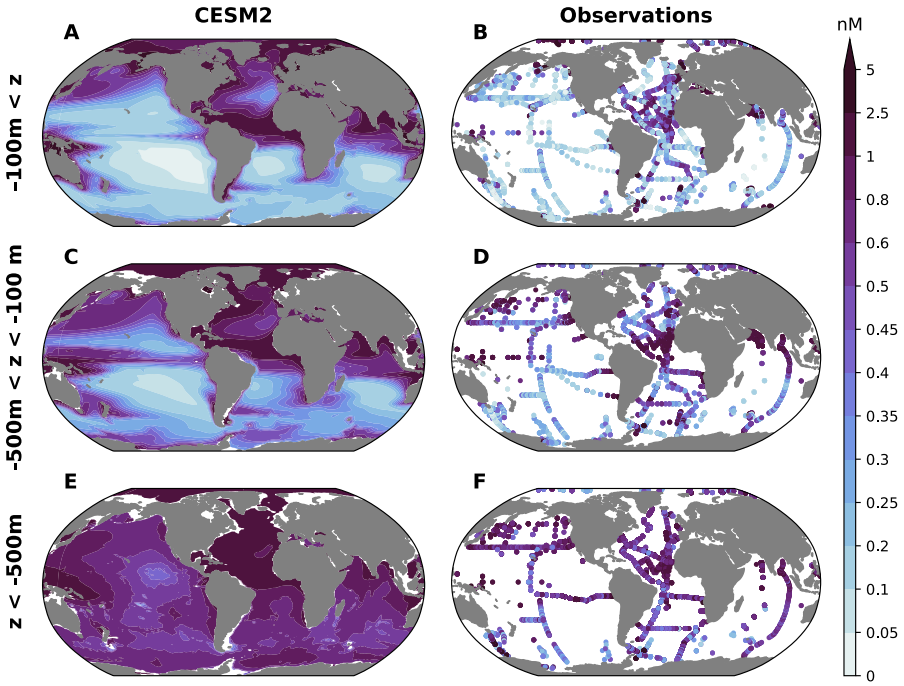

Figure 18. Dissolved iron concentrations in (left panels) CESM2 simulations over 1990–2014 and (right panels) observations from Schlitzer et al. (2018) with additional observations compiled by Tagliabue et al. (2012) and Moore and Braucher (2008). The rows show different depth ranges: (A, B) above 100 m, (C, D) between 500 m and 100 m and (E, F) below 500 m.

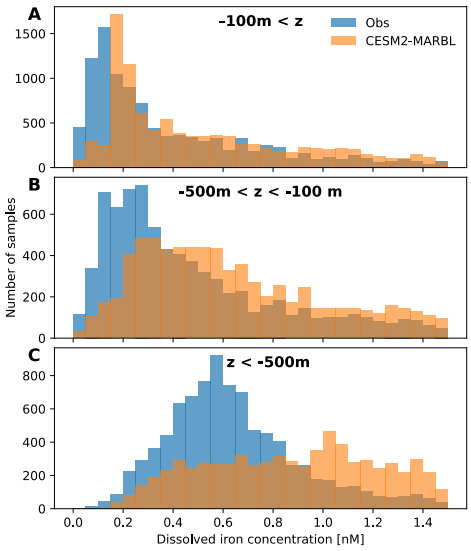

Figure 19. Histograms of dissolved iron concentrations in CESM2 simulations over 1990–2014 and observations. The model results have been sampled at the locations of the observations. The rows show different depth ranges: (A) above 100 m, (B) between 500 m and 100 m and (C) below 500 m.

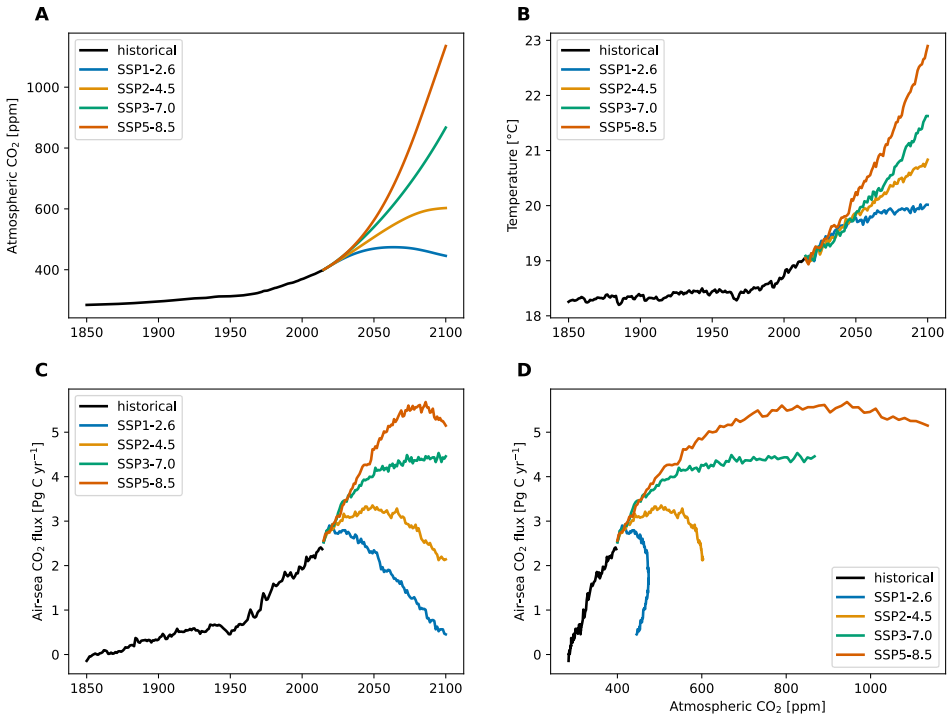

Figure 20. Time series of ensemble-mean (A) prescribed atmospheric CO_2, (B) CESM2 simulated global mean sea surface temperature, (C) globally-integrated air-sea flux. (D) Globally-integrated air-sea CO_2 flux as a function of atmospheric CO_2.

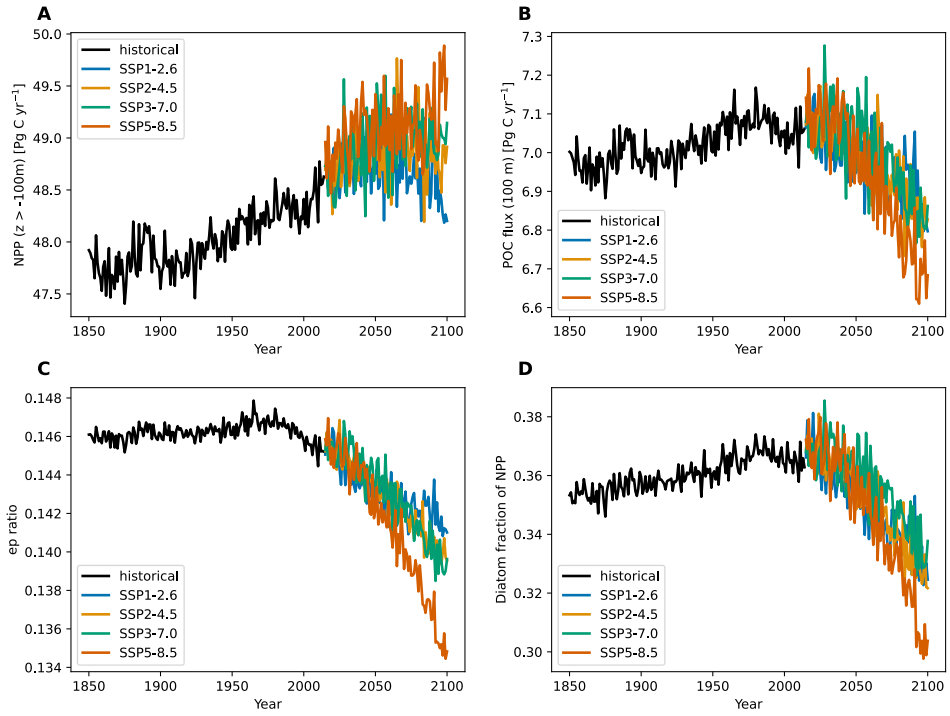

Figure 21. Globally-integrated time series of simulated (A) net primary productivity (B) particulate organic carbon (POC) export at 100 m, (C) particulate export ratio (export/NPP), and (D) the fraction of NPP accomplished by diatoms.

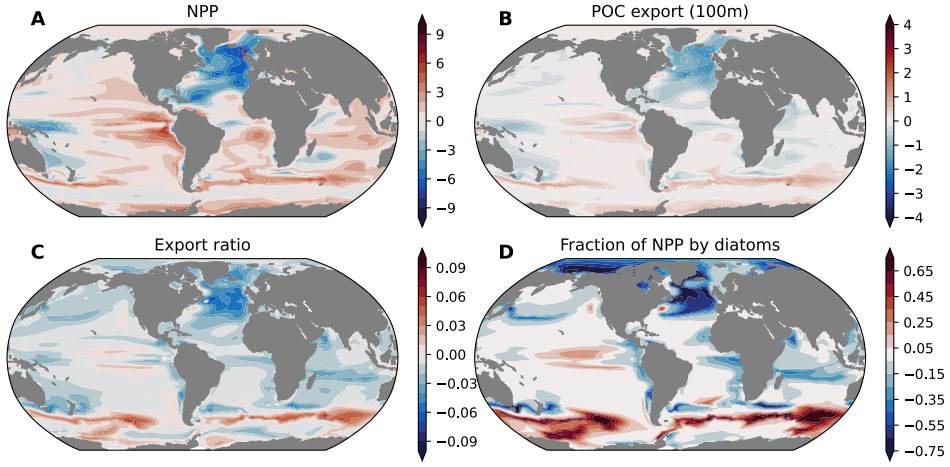

Figure 22. Change between the historical (1990–2014) and end of 21st century (2086–2100) under SSP5-8.5 for (A) net primary productivity (B) particulate organic carbon (POC) export at 100 m, (C) particulate export ratio (sinking export/NPP), and (D) the fraction of NPP accomplished by diatoms.